

Document downloaded from:

<http://hdl.handle.net/10251/60649>

This paper must be cited as:

Fernández Domene, RM.; Sánchez Tovar, R.; García Antón, J. (2014). Passive Behavior and Passivity Breakdown of AISI 304 in LiBr Solutions through Scanning Electrochemical Microscopy. *Journal of The Electrochemical Society*. 161(12):565-572. doi:0013-4651/2014/161(12)/C565/8/\$31.00.



The final publication is available at

<http://dx.doi.org/10.1149/2.1051412jes>

Copyright Electrochemical Society

Additional Information

1 **Passive Behavior and Passivity Breakdown of AISI 304 in LiBr Solutions through**  
2 **Scanning Electrochemical Microscopy**

3  
4 **R. M. Fernandez-Domene, R. Sánchez-Tovar, and J. García-Antón<sup>z</sup>**

5  
6 Ingeniería Electroquímica y Corrosión (IEC), Departamento de Ingeniería Química y  
7 Nuclear, ETSI Industriales, Universitat Politècnica de València, Camino de Vera s/n,  
8 46022 Valencia, Spain

9 <sup>z</sup>E-mail: jgarciaa@iqn.upv.es

10  
11 The passive behavior and passivity breakdown of AISI 304 stainless steel in LiBr  
12 solutions has been investigated by means of scanning electrochemical microscopy  
13 (SECM). The sample generation – tip collection (SG-TC) mode was used to operate the  
14 SECM and the tip potential was biased to detect the electroactive species. The evolution  
15 of the current at the ultramicroelectrode tip with the applied potential within the passive  
16 range was followed at different LiBr concentrations. Results show that the absolute  
17 value of the current at the tip increases with the applied potential. Additionally, SECM  
18 was also used to detect stable pits formed on the stainless steel surface in a 0.2 M LiBr  
19 solution. The results show clear evidence of the presence of high amounts of other  
20 reducible species (metal cations) apart from oxygen. Also, the dish-shape morphology  
21 of the pits observed using Confocal Laser Scanning Microscopy will be discussed in  
22 relation to the kinetics of the reactions observed using SECM.

23  
24 Manuscript submitted April 22, 2014; revised manuscript received September 5, 2014.  
25 Published xx xx, xxxx.  
26

27 **1. INTRODUCTION**

28

29 Stainless steel (SS) is a generic name commonly used for the group of iron-based alloys  
30 which are the most widely known metallic materials [1-3]. One of the main  
31 characteristics of SS is their resistance to corrosion in many environments, which is  
32 provided by a very thin and protective surface oxide film, known as passive film. It is  
33 generally accepted that passive films formed on SS have a duplex structure which  
34 consists of an inner region rich in chromium and an outer region rich in iron [4-9].  
35 Austenitic SS are the most common and familiar types of SS [2]. Among austenitic SS,  
36 type 304 SS contains approximately 18 wt. % of chromium and 8 wt. % of nickel and is  
37 widely used in chemical processing equipment, for food, dairy, and beverage industries,  
38 for heat exchangers and in the milder chemicals.

39

40 Pitting corrosion of passive metals is considered to be more dangerous than uniform  
41 corrosion, since it is more difficult to detect, predict and design against [10]. Localized  
42 breakdown of passive films leads to an enhancement of metal dissolution at the site of  
43 the pit due to the formation of a galvanic cell between the pit (anode) and the intact  
44 passive film (cathode). Therefore, pitting corrosion may result in perforation of a pipe  
45 or in structural failure [2].

46

47 Scanning Electrochemical Microscopy (SECM) has become a powerful technique for  
48 quantitative investigations of corrosion processes, including the study of pitting  
49 corrosion and other localized degradation processes [11-28]. SECM involves the use of  
50 a mobile ultramicroelectrode (UME) probe of micrometer dimension to investigate the  
51 activity and/or topography of an interface on a localized scale [29]. One of the modes of

52 SECM operation is the substrate generation/tip collection (SG/TC) mode, in which the  
53 substrate under study acts to generate species that are measured at the UME tip, which  
54 is held at a potential sufficient for a redox reaction to occur. SECM is an ideal tool for  
55 the investigation of local corrosion phenomena since it permits the possibility of  
56 precisely positioning the small UME tip close to the object under investigation, the  
57 active pit, in contrast to conventional methods frequently used to study pitting corrosion  
58 of passive metals, such as potentiodynamic polarization curves or electrochemical  
59 impedance spectroscopy (EIS).

60

61 The dissolution and pitting corrosion of iron and carbon steels [14, 22, 23, 27], as well  
62 as of stainless steels [11, 15, 17-20, 24, 28] have been investigated by SECM in several  
63 electrolytes containing  $\text{Cl}^-$  anions. However, studies on pitting corrosion of stainless  
64 steels in the presence of  $\text{Br}^-$  anions using SECM have not been found in the literature.  
65 Therefore, the aim of this study is to investigate the passive behavior and passivity  
66 breakdown of an austenitic stainless steel (AISI 304) in  $\text{Br}^-$  containing solutions by  
67 means of SECM and Confocal Laser Scanning Microscopy.

68

## 69 **2. EXPERIMENTAL PROCEDURE**

70

### 71 *2.1. Material and electrolyte*

72

73 The material tested was AISI 304 stainless steel (SS) (0.05 wt.% C, 18 wt.% Cr, 10  
74 wt.% Ni, 0.4 wt.% Si, 0.1 wt.% N, Bal. Fe). AISI 304 SS electrodes were cylindrically  
75 shaped and covered with a polytetrafluoroethylene (PTFE) coating, to expose an area of  
76  $0.5 \text{ cm}^2$  to the test solution. All specimens were wet abraded from 200 to 4000 SiC grit,

77 and finally rinsed with distilled water and air-dried. AISI 304 SS electrodes were tested  
78 in two different naturally-aerated LiBr solutions: 0.2M and 0.6M, at a constant  
79 temperature of 25° C.

80

## 81 2.2. Potentiodynamic polarization curves

82

83 Cyclic potentiodynamic polarization curves of AISI 304 SS in the LiBr solutions were  
84 determined using a SOLARTRON 1287 potentiostat. The curves were repeated at least  
85 three times in order to verify reproducibility. The working electrode potential was  
86 measured vs. a silver-silver chloride (Ag/AgCl 3M KCl) reference electrode. The  
87 auxiliary electrode was a platinum wire. Before the tests, the specimen potential was  
88 reduced to  $-0.4 V_{\text{Ag/AgCl}}$  in order to create reproducible initial conditions. Then, the  
89 electrode potential was scanned from  $-0.4 V_{\text{Ag/AgCl}}$  in the positive direction at  
90  $0.5 \text{ mV s}^{-1}$ . When the current density reached  $10 \text{ mA cm}^{-2}$ , the potential scan was  
91 reversed in order to evaluate the repassivation tendency.

92

93 From the  $E$ -log  $i$  plot, the corrosion potential ( $E_{\text{corr}}$ ) and corrosion current density ( $i_{\text{corr}}$ )  
94 were obtained. The pitting potential ( $E_p$ ) was evaluated using a criteria previously used  
95 in other studies [30], once the rapid and stable increase of the anodic current density  
96 occurs. The repassivation potential values ( $E_{rp}$ ) were taken at the crossing between the  
97 backward scan and the forward scan [31]. Passive and repassivation current densities ( $i_p$   
98 and  $i_{rp}$ , respectively) were also obtained, being  $i_p$  the current density in the passive  
99 domain and  $i_{rp}$  the current density at  $E_{rp}$ .

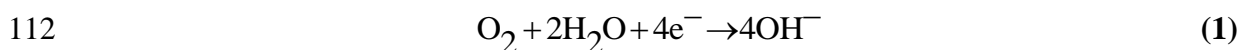
100

## 101 2.3. SECM measurements

102

103 SECM tests were performed using a Sensolytics device connected to an Autolab  
104 AUT84192 bipotentiostat. A platinum ultramicroelectrode (UME) of 25  $\mu\text{m}$  in diameter  
105 (the outer glass shield was 1.5 mm in diameter) was used as the SECM tip. Oxygen was  
106 used as the electrochemical mediator at the tip. The cyclic voltammogram was recorded  
107 at a scan rate of 50  $\text{mV s}^{-1}$  from 0  $\text{V}_{\text{Ag}/\text{AgCl}}$  to  $-1.2 \text{ V}_{\text{Ag}/\text{AgCl}}$ . **Figure 1** shows the cyclic  
108 voltammogram of  $\text{O}_2$  in the 0.2 M LiBr solution using the 25  $\mu\text{m}$  platinum UME. A  
109 wide current plateau can be observed at potential values between  $-0.5 \text{ V}_{\text{Ag}/\text{AgCl}}$  and  $-1$   
110  $\text{V}_{\text{Ag}/\text{AgCl}}$ , approximately, corresponding to the oxygen reduction reaction:

111



113

114 The curve displayed in **Figure 1** was used to choose the potential of the UME tip, which  
115 was set at  $-0.7 \text{ V}_{\text{Ag}/\text{AgCl}}$  to enable the diffusion-limited reduction of oxygen at the tip.

116

117 To study the influence of the applied potential on the passive behavior of AISI 304 SS,  
118 passive films were formed on its surface imposing different potentials within the  
119 passive range (0.0, 0.1 and  $0.2 \text{ V}_{\text{Ag}/\text{AgCl}}$ ) for 1 hour.

120

121 The reduction of oxygen on the microelectrode was used to establish the height of the  
122 tip over the AISI 304 SS sample. After passive film formation, approach curves  
123 representing Current (I) vs. Distance between the UME tip and the surface of the sample  
124 (Z) were performed to select the best height of the UME tip. As an example, **Figure 2**  
125 shows an approach curve for the tip polarized at  $-0.7 \text{ V}_{\text{Ag}/\text{AgCl}}$  with the sample potential  
126 set at 0.0 V in the 0.2 M LiBr solution. The zero position of the tip, that is, the point

127 where the approach curves began, was an arbitrary position such that the influence of  
128 the specimen on the probe response was not significant. From this zero position the  
129 UME was moved down towards the sample and it stopped when the tip current reached  
130 75% of the initial value in the bulk solution [25]. In order to prevent the tip from  
131 scratching the AISI 304 SS surface, due to roughness or small tilt of the sample, the  
132 distance between the UME and the substrate surface was afterwards increased by 5  $\mu\text{m}$ .  
133 This increase in the tip-substrate distance by 5  $\mu\text{m}$  resulted in an increase in the tip  
134 current by 8.33 %, in absolute value. Then, SECM scans were obtained by positioning  
135 the UME tip directly above and perpendicular to the sample and scanning the surface at  
136 steps of 250  $\mu\text{m}$  in the X and Y directions. The scanned dimensions were 2000  $\mu\text{m}$   $\times$   
137 2000  $\mu\text{m}$  and the scan rate was 50  $\mu\text{m s}^{-1}$ .

138

139 To study the initiation and formation of stable pits on the surface of the AISI 304 SS in  
140 the 0.2 M LiBr solution, the sample was subsequently biased at 0.45  $V_{\text{Ag}/\text{AgCl}}$ , a  
141 potential close to the pitting potential. After the appearance of the first stable pit,  
142 different line scans were performed at different times by shifting the UME tip 3000  $\mu\text{m}$   
143 along the X direction passing just above the pit, at steps of 250  $\mu\text{m}$ . Although the step  
144 size was significantly bigger than the tip diameter, this approach is acceptable in this  
145 case because the aim of the present work is not to resolve the surface to evidence  
146 precursor sites for pit nucleation, but to follow the propagation stages of a stable pit  
147 once nucleated. The tip potential remained set at -0.7  $V_{\text{Ag}/\text{AgCl}}$  to detect the electroactive  
148 species (metal cations) released from the localized corrosion site by reducing them at  
149 the UME tip, thus obtaining a cathodic current related to the activity within the pit.  
150 Using this mode of SECM operation, called sample generation – tip collection (SG-TC),  
151 the use of electrochemical mediators (i.e., an oxidizable/reducible species) that could

152 interact with the substrate, such as the redox couple  $\Gamma/\Gamma_3^-$ , is avoided, thus eliminating  
153 their interference with the corrosion reactions [11, 25, 29]. A 3D map of the surface  
154 around the pit was also obtained through scanning the surface at steps of 500  $\mu\text{m}$  in the  
155 X and Y directions. The scanned dimensions were 3000  $\mu\text{m}$   $\times$  2000  $\mu\text{m}$  in X and Y,  
156 respectively, with a scan rate of 50  $\mu\text{m s}^{-1}$ .

157

158 After studying the formation and growth of a stable pit on the AISI 304 SS, the sample  
159 polarization was stopped to study pit repassivation at open circuit potential. Line scans  
160 and a 3D map of the surface were also obtained, following the same procedure  
161 explained above.

162

#### 163 *2.4. Confocal Laser Scanning Microscope measurements*

164

165 After potentiodynamic polarization curves, the AISI 304 SS samples were rinsed and  
166 examined with a Confocal Laser Scanning Microscope (CLSM) Olympus LEXT  
167 OLS3100, which uses the LEXT OLS 6.0.3 software. The CLSM uses a Laser Diode  
168 with a wavelength of 408 nm, an outstanding horizontal resolution of 0.22  $\mu\text{m}$ , vertical  
169 resolution of 0.01  $\mu\text{m}$  (z-axis), and a magnification range from 120x to 14400x.

170

171 The morphology of the pit formed on the AISI 304 SS electrode after the SECM  
172 measurements was also examined using the CLSM. The average pit radius and pit depth  
173 were quantified with the CLSM.

174

175

### 176 **3. RESULTS AND DISCUSSION**



177

178 *3.1. Potentiodynamic polarization curves*

179 **Table 1** shows the parameters determined from polarization curves (**Figure 3**) at two  
180 different LiBr concentrations: 0.2M and 0.6M. As it can be seen in Table 1, an increase  
181 in LiBr concentration from 0.2M to 0.6M slightly shifts corrosion potentials to more  
182 active values and enhances corrosion current densities.

183 Polarization curves also provide information about the pitting, passivation and  
184 repassivation behavior of the material. AISI 304 is susceptible to pitting corrosion since  
185 bromides are very aggressive ions that promote SS passive film breakdown [30, 32, 33].  
186 The lowest  $E_p$  determined in the 0.6M LiBr solution indicates that bromides promote a  
187 decrease in the pitting corrosion resistance and, consequently, the breakdown of the  
188 passive film and the initiation of pits occur at less positive potentials.

189 **Table 1** shows that passive current densities are higher in the LiBr solution that  
190 contains more bromides. **Table 1** also shows that repassivation current densities  
191 obtained in both LiBr solutions are statistically the same. Since  $i_{rp}$  is a measure of the  
192 ability of materials to repassivate and, hence, of the extent of propagation once  
193 corrosion has initiated, the previous results indicate that the ability of AISI 304 to  
194 repassivate is essentially the same in both LiBr solutions. Additionally,  $E_{rp}$  gives  
195 information about the repassivation of the material after pitting; i.e., above  $E_{rp}$  pits that  
196 have initiated will continue to grow and at potentials below  $E_{rp}$  pits repassivate. In the  
197 present case, the corrosion potential is below  $E_{rp}$ , so pits can repassivate at potentials  
198 between  $E_{corr}$  and  $E_{rp}$ .

199 The surfaces of the stainless steel after the tests were examined with the CLSM. The  
200 number of pits together with their diameter is considerably greater in the test performed  
201 in the most concentrated solution, that is,  $\text{Br}^-$  ions increase the pitting corrosion rate  
202 [34]. This result is in agreement with the parameters determined from polarization  
203 curves.

204

### 205 *3.2. Influence of passivation potential studied by SECM*

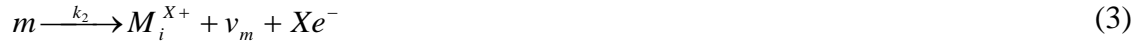
206

207 **Figure 4** shows the 3D maps of the AISI 304 SS surface biased at three different  
208 potentials among the passive range, i.e. 0, 0.1 and 0.2  $V_{\text{Ag}/\text{AgCl}}$  whereas the tip potential  
209 was set at  $-0.7 V_{\text{Ag}/\text{AgCl}}$ . **Figure 4(a)** and (b) represent the evolution of the current at the  
210 UME tip in the 0.2M and 0.6M LiBr solutions, respectively. The images correspond to  
211  $2000 \mu\text{m} \times 2000 \mu\text{m}$  in  $X$  and  $Y$  directions. The plot in **Figure 4(a)** shows that current  
212 values determined at the UME tip are higher (in absolute value), compared to those  
213 obtained in the most concentrated LiBr solution (**Figure 4(b)**). This result seems to be  
214 reasonable since the solubility of oxygen diminishes with salinity (the experimental  
215 Henry's Law constants for oxygen in the 0.2M and 0.6M LiBr solutions at atmospheric  
216 pressure and  $25^\circ \text{C}$  are  $4.54 \cdot 10^4 \text{ atm.}$  and  $4.76 \cdot 10^4 \text{ atm.}$ , respectively) [35]. Additionally,  
217 the current at the UME tip follows the same tendency with the applied potential in both  
218 concentrations; that is, it increases (in absolute value) as the potential is raised. The  
219 same tendency of the tip current obtained in both concentrations represents the  
220 reproducibility of the tests.

221 Passive films generally form as bilayers, with a highly disordered "barrier" layer  
222 adjacent to the metal and an outer film consisting of a precipitated phase that may  
223 incorporate anions and/or cations from the solution. Passivity is mainly attributed to the

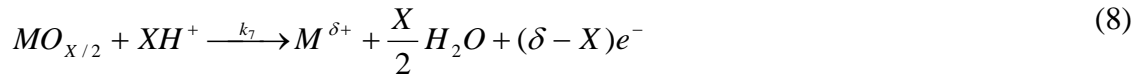
224 barrier layer [36]. The passive films formed on stainless steels are considered highly  
225 doped semiconductors with dopant or defect densities [4, 37-39]. The protectiveness of  
226 the passive film is affected by the density of dopants or charge carriers and the latter is  
227 dependent on the applied potential in the passive domain. The passive film thus  
228 constitutes a barrier layer to ion transfer but not to electron transfer. Any redox electron  
229 transfer reaction is therefore allowed to occur on the passive film-covered metal surface  
230 just like on the metal surface without any film [40]. In fact, it is well known that the  
231 reduction of oxygen takes place in the formation of the passive film as cathodic reaction  
232 [41-43]. In this way, during the formation of the passive films, i.e. at the applied  
233 potentials shown in **Figure 4**, there should be a competition between the oxygen  
234 consumed in the corresponding cathodic reaction at the passive film on the stainless  
235 steel and at the UME tip. Taking into consideration that higher potentials promote an  
236 increase in the redox reaction rates [44, 45], a gradual decrease (in absolute value) in the  
237 tip current value with the applied potential, due to an increase of the oxygen reaction in  
238 the cathodic regions of the passive film, should be shown in **Figure 4**. However, **Figure**  
239 **4** shows an opposite trend, that is, as the applied potential in the passive domain is  
240 increased, the current at the UME tip increases in absolute value. Therefore, the increase  
241 in absolute value of the tip current with the applied potential cannot be explained due to  
242 the presence of oxygen. Hence, other redox species that are influenced by the applied  
243 potential are interfering in the tip current. According to the Point Defect Model (PDM)  
244 [36, 46] the transmission of ions through the barrier layer occurs by vacancy motion,  
245 due to the preponderance of Schottky defects. Then, the following reactions may occur  
246 at the metal/film and film/solution interfaces [36, 47, 48]:

247 - Reactions at the metal/film interface:



248

249 - Reactions at the film/solution interface:



250

251 where  $m$  is a metal atom,  $V_M^{X'}$  is a cation vacancy in the passive film,  $M_i^{X+}$  is an  
 252 interstitial cation,  $M_M$  is a metal cation in a cation site of the film,  $v_m$  is a cation vacancy  
 253 in metal phase,  $V_O^{\bullet\bullet}$  is an anion vacancy in the passive film,  $O_O$  is an oxygen ion in the  
 254 passive film,  $M^{\delta+}$  is a metallic cation in the electrolyte and  $MO_{X/2}$  is the stoichiometric  
 255 passive film ( $X$  is the oxidation state of the cations in the passive film and  $\delta$  is the  
 256 oxidation state of the cations in the solution).

257

258 As the applied potential on the passive region of the stainless steel is increased, the rate  
 259 of the redox reactions is affected. Therefore, according to the reactions proposed in the  
 260 PDM, oxidation equations 2 to 6 and 8 could take place. However, in the system  
 261 proposed in this research, the charge of the cations in the oxides that form the passive

262 film ( $X$ ) is equal to the charge of these cations in the solution ( $\delta$ ), hence only reactions  
263 shown in equations 2 to 4 occurring at the metal/film interface involve an exchange of  
264 electrons. The rate of the aforementioned redox reactions will increase as the applied  
265 potential is also increased [44, 45]. Thus, increasing the potential increases the rates of  
266 formation of metallic cations in the film ( $M_M$ , in equations 2 and 4) and of interstitial  
267 cations ( $M_i^{X+}$  in equation 3). Furthermore, when the presence of these species in the  
268 passive film increases, the rate of the reactions taking place at the film/solution interface  
269 can be enhanced (equations 5 and 6), leading therefore to the formation of metallic  
270 cations in the solution ( $M^{\delta+}$ ). As the number of metallic cations ejected from the metal  
271 to the solution increases, the current at the UME tip might also increase (in absolute  
272 value) and at its applied potential ( $-0.7 V_{Ag/AgCl} = -0.495 V_{NHE}$ ), the cations that reach  
273 the tip may be reduced.

274

275 The species that are present in the studied system are oxygen, water, bromide anions  
276 ( $Br^-$ ) and lithium cations ( $Li^+$ ) of the electrolyte and those cations coming from the  
277 passive film of the stainless steel. The  $Br^-$  anions cannot be further reduced and the  $Li^+$   
278 cannot be reduced at the potential applied at the UME tip ( $E_{Li^+/Li}^0 = -3.05 V_{NHE}$ ).  
279 Moreover, neither water may be reduced to  $H_2$  ( $E_{H_2O^+/H_2}^0 = -0.83 V_{NHE}$ ). Nevertheless,  
280 as it was previously mentioned, oxygen in neutral or alkaline media might be reduced to  
281  $OH^-$  ( $E_{O_2/OH^-}^0 = 0.40 V_{NHE}$ ), but oxygen reduction cannot explain the results shown in  
282 **Figure 4**, as mentioned above. On the other hand, the main elements present in the AISI  
283 304 (iron, chromium and nickel), may be in their different oxidation states depending on  
284 the applied potential among the passive region ( $0$  to  $0.2 V_{Ag/AgCl} = 0.21-0.41V_{NHE}$ ).  
285 Therefore, all the reactions with a standard electrode potential (reduction potential)  
286 lower than the applied passive potential might take place in the oxidation direction, that

287 is, the reduced form of the pair with lower potential will be oxidized. According to the  
 288 standard electrode potentials, the iron, chromium and nickel species are stable at 0.21-  
 289  $0.41 V_{\text{NHE}}$  are  $\text{Fe}^{+3}$  ( $E^0_{\text{Fe}^{3+}/\text{Fe}} = -0.036 V_{\text{NHE}}$ ),  $\text{Fe}^{+2}$  ( $E^0_{\text{Fe}^{2+}/\text{Fe}} = -0.44 V_{\text{NHE}}$ ),  $\text{Ni}^{+2}$  ( $E^0_{\text{Ni}^{2+}/\text{Ni}}$   
 290  $= -0.23 V_{\text{NHE}}$ ) and  $\text{Cr}^{+3}$  ( $E^0_{\text{Cr}^{3+}/\text{Cr}} = -0.73 V_{\text{NHE}}$ ). Thus, from a thermodynamic point of  
 291 view the cations ejected from the passive film formed on the stainless steel in our study  
 292 may be  $\text{Fe}^{+2}$ ,  $\text{Fe}^{+3}$ ,  $\text{Ni}^{+2}$  and  $\text{Cr}^{+3}$ . Then, in order to relate the current at UME tip with  
 293 the reduction of some species, it is necessary to know which of the aforementioned  
 294 cations would be reduced at  $-0.7 V_{\text{Ag}/\text{AgCl}} = -0.495 V_{\text{NHE}}$ , i.e. the potential held at the  
 295 UME tip. Any reduction reaction with a standard electrode potential higher than  $-0.495$   
 296  $V_{\text{NHE}}$  might take place in our system. The following reactions may occur:

297



298

299 Note that in order to reduce  $\text{Cr}^{3+}$  to metallic Cr, more negative potentials are needed  
 300 ( $-0.73 V_{\text{NHE}}$ ).

301 According to the literature [7, 8, 49] nickel has not been found in the composition of  
 302 AISI 304 or AISI 316 SS passive films. Hence, the possible reactions at the UME tip  
 303 (apart from the reduction of  $\text{O}_2$  to  $\text{OH}^-$ , which is always present in our system, see  
 304 **Figure 1**) are those involving iron species ( $\text{Fe}^{+2}$  and  $\text{Fe}^{+3}$ ). In this way, a logical  
 305 explanation of the tendency observed in **Figure 4** (i.e., the current of the UME tip  
 306 increases in absolute value as the potential also increases), might be the higher amount  
 307 of iron cations ejected from the passive film and available at the UME tip due to an

308 increase in the applied potential. Then, at higher potentials more cations are reduced to  
309 iron (equations 8 and 10) at the UME tip which is held at  
310  $-0.7 V_{\text{Ag/AgCl}}$  [14].

311

### 312 *3.3. SECM imaging of active pitting corrosion and repassivation*

313

314 To study the initiation and formation of stable pits on the surface of the AISI 304 SS in  
315 0.2 M LiBr solution, different potentials were selected and applied to the substrate (in  
316 the passive region but close to the value of  $E_p$  determined from polarization curves in  
317 **Figure 3**). The lowest potential at which a stable pit appeared was  $0.45 V_{\text{Ag/AgCl}}$ , so the  
318 sample was biased at this value. After the appearance of the first stable pit, different line  
319 scans of  $3000 \mu\text{m}$  each were performed just above the pit, setting the UME tip potential  
320 at  $-0.7 V_{\text{Ag/AgCl}}$ . To perform these experiments, a test solution of 0.2 M LiBr has been  
321 chosen instead of 0.6 M LiBr to minimize the appearance of pits on the electrode  
322 surface when imposing a potential close to  $E_p$ .

323

324 **Figure 5** shows the line scans at different polarization times. It can be observed that,  
325 regardless of the polarization time, the currents recorded when the tip passed just over  
326 the center of the pit ( $X = 1500 \mu\text{m}$ ) were significantly higher (in absolute value) than  
327 the currents measured over the areas covered with an undamaged passive film. Souto et  
328 al [25, 26], working with polymer-coated carbon steel plates, also observed an increase  
329 in the current measured at the tip when it passed over a circular defect artificially  
330 produced in the organic coating. They explained these results in terms of an  
331 enhancement of the amount of soluble oxygen available from the electrolyte volume  
332 inside the hole, since the substrate surface was no longer obstructing the diffusion of

333 oxygen from the bulk. Consequently, the currents measured at the UME tip over the  
334 defect were of the same order of magnitude as that recorded in the bulk solution for  
335 oxygen reduction. In the present case, however, currents recorded at the tip near the  
336 active pit were far more negative than those observed in the bulk solution associated  
337 with the reduction of oxygen at the UME tip (which are of the order of -2 nA, see  
338 **Figure 2**).

339

340 On the other hand, since a process of active corrosion was taking place inside the pit  
341 (the current of the substrate increased drastically just before the appearance of the stable  
342 pit), a redox competition for dissolved oxygen could be expected to occur inside the pit  
343 between the UME tip and the bare steel surface. According to Souto et al [21, 25, 26],  
344 the concentration of oxygen available to be reduced at the tip will decrease near a  
345 corroding surface, such as inside an active pit, due to the appearance of cathodic sites  
346 where oxygen can be consumed. Assuming that it is the O<sub>2</sub> reduction reaction that is  
347 taking place at the tip, a decrease in the amount of oxygen available at the tip would  
348 lead to a decrease (in absolute value) in the tip current. However, such a decrease in the  
349 tip current near the active pit with respect to the background current is not observed in  
350 **Figure 5**.

351

352 Inside a stable pit the characteristics of the electrolyte are different from those in bulk  
353 solution [31]. The local environment becomes enriched in metal cations and anionic  
354 species such as bromides or chlorides, and the pH is lower owing to cation hydrolysis.  
355 This fact makes pitting autocatalytic, that is, once a pit becomes stable, it grows at an  
356 ever-increasing rate without any external stimulus [2, 31]. During active corrosion of  
357 iron and stainless steels (such as AISI 304 SS), Fe<sup>2+</sup> cations are produced inside the pits



358 [11, 14, 24, 50]. Other cations such as  $\text{Cr}^{3+}$  and  $\text{Ni}^{2+}$  can also be produced inside active  
359 pits formed on stainless steels [28, 51]. The high currents measured at the UME tip  
360 when it was located just over the pit suggest an active corrosion process inside the pit  
361 releasing metal cations and a subsequent reduction of those cations at the UME tip [11,  
362 14], which was biased at  $-0.7 \text{ V}_{\text{Ag}/\text{AgCl}}$ . Protons may also be simultaneously reduced at  
363 the tip [14, 52].

364

365 To confirm the explanations given above concerning the reduction process taking place  
366 at the tip, **Figure 6** shows a cyclic voltammogram taken while the tip was positioned  
367 near the active corrosion pit. Comparing the voltammogram after corrosion with that  
368 recorded in the solution bulk before corrosion (initial in **Figure 6**), it can be clearly  
369 observed that cathodic currents greatly increased after the corrosion process. This result  
370 indicates the presence of high amounts of other reducible species (metal cations) apart  
371 from oxygen.

372

373 It can be observed from **Figure 5(a)** that at short polarization times the tip current  
374 reached very negative and approximately constant values, but it started decreasing after  
375 70 seconds. This behavior can be explained taking into account the precipitation of a  
376 salt film on the pit surface [31, 51, 53, 54]. The high cathodic currents recorded at short  
377 polarization times imply a very high metal dissolution rate (in fact, higher than the  
378 diffusion rate of cations from the pit towards the UME tip) leading to an increase in the  
379 ionic concentration inside the pit and to eventually reaching supersaturation conditions  
380 [31, 51]. This salt layer decreased metal dissolution since it acted as a diffusion barrier  
381 and hence the process of pit growth became limited by mass transport.

382

383 However, at longer polarization times (from 210 seconds on), the tip current began to  
384 increase again (**Figure 5(b)**) although it never reached values as high as those measured  
385 at the beginning of the test, when metal dissolution was very intense. **Figure 7**  
386 compares the values of the tip current measured just over the active pit at  $X = 1500 \mu\text{m}$   
387 at different polarization times. It can be observed that  $I_{\text{pit}}$  values were very high in the  
388 beginning (in absolute value), indicating a very fast dissolution inside the active pit  
389 which led to an increase in the concentration of metal cations inside the pit (A in **Figure**  
390 **7**) [31, 51]. Eventually, supersaturation conditions were reached and a solid salt layer  
391 formed on the pit surface, leading to a considerable decrease in the tip current over the  
392 pit (B in **Figure 7**) [31, 51]. After the sudden drop in  $I_{\text{pit}}$  due to the precipitation of the  
393 salt film on the pit surface, the current value increased again following a linear tendency  
394 with time (C in **Figure 7**). This displacement of current towards higher values (in  
395 absolute value) with increasing polarization time is consistent with an active process of  
396 corrosion taking place inside the pit and is directly related to pit propagation [23].  
397 Moreover, the previous results imply that after 210 seconds of active pitting corrosion,  
398 the salt layer formed on the pit surface no longer acted as a diffusion barrier, since a  
399 continuous increase in the release of metallic cations from the active pit and their  
400 subsequent reduction at the UME tip was observed.

401

402 It is worth mentioning that an increase in the background current with increasing  
403 polarization times can be observed in **Figure 5**, which is associated with the  
404 accumulation and slow diffusion of metallic cations released from the substrate towards  
405 the bulk solution [24, 55]. Hence, at long polarization times, small amounts of these  
406 cations can be reduced at the UME tip far from the pit. However, the ratio between the  
407 current over the active pit and the background current is very high and it increases with

408 immersion time, which indicates that changes in the background current with time are  
409 very small compared to the changes of the tip current measured above the active pit.

410

411 Once the growth of the active pit with time has been studied, the next step is to study  
412 the repassivation of the pit when stopping potentiostatic polarization. As in the previous  
413 case, different line scans were carried out above the repassivating pit, with the tip  
414 potential set at  $-0.7 V_{Ag/AgCl}$  and leaving the AISI 304 SS substrate at open circuit  
415 potential. **Figure 8** shows the line scans at different repassivation time.

416

417 It can be observed from **Figure 8(a)** that immediately after stopping polarization the  
418 cathodic current measured at the UME tip sharply decreased (in absolute value). After  
419 that (**Figure 8**) the tip current measured above the pit became less negative with  
420 repassivation time until it reached approximately constant values along the scan length  
421 after 160 seconds. These results reveal a total repassivation of the existing pit, since its  
422 propagation ceased completely. Final values of the tip current are slightly higher than  
423 those recorded before the onset of pitting corrosion on the substrate at  $0.45 V_{Ag/AgCl}$ . As  
424 it has been mentioned above, this difference in background current with time is  
425 explained by the gradual accumulation of metallic cations released from the metal  
426 substrate.

427 The previous results show that the pit formed on AISI 304 SS under potentiostatic  
428 polarization was no longer stable at open circuit potential and stopped propagating. Pit  
429 stability depends, among other things, on the maintenance of pit electrolyte composition  
430 and pit bottom potential [31, 56]. If a salt film is formed on the pit bottom, the pit  
431 growth rate will be diffusion controlled. Under these circumstances, a decrease in the  
432 potential may not lead to repassivation and pits may continue to grow, depending on the

433 composition of the pit electrolyte [31, 56]. The formation of a salt film has been cited  
434 above as a likely reason to explain the decrease in the tip current with polarization time  
435 after reaching very negative values (**Figure 5(a)** and **Figure 7**). However, at longer  
436 polarization times (from 210 seconds on) the salt layer no longer influenced pit growth,  
437 since the current associated with the cations released from the pit bottom started to  
438 increase again (in absolute value) (**Figure 7**). Therefore, the complete repassivation of  
439 the dissolving metal surface at the pit bottom after 160 seconds at open circuit potential  
440 indicates that, in the system under study and after some time of potentiostatic pit  
441 growth, charge-transfer processes inside the pit played an essential role in its stability.

442

443 **Figure 9** shows the 3D maps of the AISI 304 SS surface obtained at the end of the pit  
444 activation process at  $0.45 V_{\text{Ag}/\text{AgCl}}$  (**Figure 9(a)**) and at the end of the pit repassivation  
445 process at open circuit potential (**Figure 9(b)**). The images represent  $3000 \mu\text{m} \times 2000$   
446  $\mu\text{m}$  in  $X$  and  $Y$  directions, respectively. The plot in **Figure 9(a)** clearly shows the  
447 generation and release of metal cations from a single pit centered in the point ( $X = 1500$   
448  $\mu\text{m}$ ;  $Y = 1000 \mu\text{m}$ ) and reduced afterwards at the UME tip, whose potential was set at  
449  $-0.7 V_{\text{Ag}/\text{AgCl}}$ . It can be observed from **Figure 9(b)** that the formation of  $\text{Fe}^{2+}$  and other  
450 cationic species from the pit was effectively stopped at open circuit potential, since at  
451 the point ( $X = 1500 \mu\text{m}$ ;  $Y = 1000 \mu\text{m}$ ) the tip current was similar to the background  
452 current, indicating a complete repassivation of the pit.

453

454 **Figure 10** shows the 2D image of the pit formed on the AISI 304 SS surface in 0.2 M  
455 LiBr solution at  $0.45 V_{\text{Ag}/\text{AgCl}}$ , obtained with a CLSM. In order to visualize the pit  
456 morphology and to quantify its depth, two profiles (longitudinal and transversal) were  
457 also obtained. It can be observed from the 2D image (**Figure 10(a)**) that the pit mouth

458 had an approximately equiaxed (circular) shape, bounded by facets. According to  
459 Newman and Franz, it is possible that this pit grew initially by coalescence from several  
460 nucleation points [51]. The average radius of the pit was estimated to be  $99.8 \pm 0.7 \mu\text{m}$ .  
461 It can also be observed from both profiles (**Figures 10(b)** and **10(c)**) that the bottom of  
462 the pit was not uniform. The average pit depth was  $8.0 \pm 0.9 \mu\text{m}$ .

463

464 It is evident from the above calculations that the pit radius was far higher than the pit  
465 depth, indicating that this pit was not hemispherical but dish-shaped. Some authors  
466 working with stainless steels have observed a change in the pit shape from  
467 hemispherical to dish-shaped during their growth [57-61]. According to Newman [58,  
468 60, 61], early pit growth takes place in a hemispherical mode under the remnants of an  
469 overhanging passive film; when a pit reaches a critical size, this cover is destroyed and  
470 the hemispherical cavity is opened to the bulk solution. Hence, large pits (of the order of  
471 several tens or even hundreds of  $\mu\text{m}$  in diameter) have been usually found to be dish-  
472 shaped rather than perfectly hemispherical, because the absence of a pit cover makes the  
473 hemispherical shape unstable, resulting in a faster dissolution rate at the pit edges [31,  
474 58, 60-63]. These explanations are consistent with the SECM and CLSM observations  
475 of the pit formed on AISI 304 SS, which presented a dish-shaped morphology.

476

## 477 **CONCLUSIONS**

478

479 An increase in LiBr concentration from 0.2M to 0.6M enhances the passive current  
480 density and lowers the pitting potential.

481

482 As the applied potential in the passive domain is increased, the current at the UME tip  
483 increases in absolute value. This increase can be explained due to the enhancement of  
484 metallic cations at the film/solution interface at high potentials, according to the Point  
485 Defect Model. As the number of metallic cations ejected from the metal to the solution  
486 increases, the current at the UME tip might also increase.

487

488 The tip currents recorded over the center of the pit were significantly higher (in absolute  
489 value) than the currents measured over the areas covered with an undamaged passive  
490 film. This fact can be explained by an active corrosion process taking place inside the  
491 pit, resulting in the release of metal cations and their subsequent reduction at the UME  
492 tip.

493

494 The evolution of the tip current over the active pit with polarization time suggested a  
495 very high metal dissolution rate during the first 70 seconds and then the precipitation of  
496 a salt film on the pit surface after reaching supersaturation conditions. At longer  
497 polarization times the tip current began to increase again indicating that an active  
498 corrosion process was occurring inside the pit.

499

500 Immediately after stopping polarization the cathodic current measured at the UME tip  
501 sharply decreased (in absolute value) and became less negative with repassivation time  
502 until it reached approximately constant values. These results reveal a total repassivation  
503 of the existing pit.

504

505 The pit radius was observed to be far higher than the pit depth, indicating that this pit  
506 was not hemispherical but dish-shaped. This morphology is consistent with the loss of

507 the pit cover (a salt layer or the remnants of an overhanging passive film) and the  
508 preferential dissolution at the pit edges, leading to a change in pit shape from perfectly  
509 hemispherical at the first stages of pit growth to a dish-shaped form at longer times.

510

## 511 **ACKNOWLEDGEMENTS**

512 The authors would like to express their gratitude to the Generalitat Valenciana for its  
513 help in the SECM acquisition (PPC/2011/013) and in the CLSM acquisition  
514 (MY08/ISIRM/S/100) and to Dr. Asuncion Jaime for her translation assistance.

515

## 516 **REFERENCES**

517

518 [1] Harold M.Cobb (Ed.), Steel Products Manual: Stainless Steels, Iron & Steel  
519 Society, 1999.

520 [2] P. A. Schweitzer, Corrosion Engineering Handbook: Fundamentals of Metallic  
521 Corrosion, CRC Press, Boca Ratón, FL., 2007.

522 [3] A. J. Sedriks, Corrosion Resistance of Stainless Steels and Nickel Alloys, in:  
523 S.D. Cramer, B.S. Covino, Jr. (Eds.), Corrosion: Fundamentals, Testing and  
524 Protection, Vol. 13A, ASM Handbook, ASM International, Materials Park,  
525 OH, 2003, p. 697-702.

526 [4] N. E. Hakiki, S. Boudin, B. Rondot, M. Da Cunha Belo. The electronic  
527 structure of passive films formed on stainless steels, Corros. Sci. 37 (1995)  
528 1809-1822.

- 529 [5] T. L. S. Wijesinghe, D. J. Blackwood. Photocurrent and capacitance  
530 investigations into the nature of the passive films on austenitic stainless steels,  
531 *Corros. Sci.* 50 (2008) 23-34.
- 532 [6] N. E. Hakiki, M. Da Cunha Belo, A. M. P. Simões, M. G. S. Ferreira.  
533 Semiconducting Properties of Passive Films Formed on Stainless Steels, *J.*  
534 *Electrochem. Soc.* 145 (1998) 3821-3829.
- 535 [7] I. Olefjord, B. Brox, U. Jelvestam. Surface Composition of Stainless Steels  
536 during Anodic Dissolution and Passivation Studied by ESCA, *J. Electrochem.*  
537 *Soc.* 132 (1985) 2854-2861.
- 538 [8] G. Lothongkum, S. Chaikittisilp, A. W. Lothongkum. XPS investigation of  
539 surface films on high Cr-Ni ferritic and austenitic stainless steels, *Appl. Surf.*  
540 *Sci.* 218 (2003) 203-210.
- 541 [9] L. Freire, M. J. Carmezim, M. G. S. Ferreira, M. F. Montemor. The passive  
542 behavior of AISI 316 in alkaline media and the effect of pH: A combined  
543 electrochemical and analytical study, *Electrochim. Acta* 55 (2010) 6174-6181.
- 544 [10] P. R. Roberge, *Corrosion Engineering. Principles and Practice*, 1<sup>st</sup>. ed.,  
545 McGraw-Hill, New York, NY, 2008.
- 546 [11] D. O. Wipf, Initiation and study of localized corrosion by scanning  
547 electrochemical microscopy, *Colloid Surface A* 93 (1994) 251-261.
- 548 [12] N. Casillas, S. Charlebois, W. H. Smyrl, H. S. White, Pitting Corrosion of  
549 Titanium, *J. Electrochem. Soc.* 141 (1994) 636-642.



- 550 [13] S. B. Basame, H. S. White, Scanning Electrochemical Microscopy of Native  
551 Titanium Oxide Films. Mapping the Potential Distribution of Spatially-  
552 Localized Electrochemical Reactions, *J. Phys. Chem.* 99 (1995) 16430-16435.
- 553 [14] J. W. Still, D. O. Wipf, Breakdown of the Iron Passive Layer by Use of the  
554 Scanning Electrochemical Microscope, *J. Electrochem. Soc.* 144 (1997) 2657-  
555 2665.
- 556 [15] Y. Zhu, D. E. Williams, Scanning Electrochemical Microscopic Observation of  
557 a Precursor State to Pitting Corrosion of Stainless Steel, *J. Electrochem. Soc.*  
558 144 (1997) L43-L45.
- 559 [16] S. B. Basame, H. S. White, Scanning electrochemical microscopy:  
560 measurement of the current density at microscopic redox-active sites on  
561 titanium, *J. Phys. Chem. B* 102 (1998) 9812-9819.
- 562 [17] D. E. Williams, T. F. Mohiuddin, Y. Y. Zhu, Elucidation of a Trigger  
563 Mechanism for Pitting Corrosion of Stainless Steels Using Submicron  
564 Resolution Scanning Electrochemical and Photoelectrochemical Microscopy,  
565 *J. Electrochem. Soc.* 145 (1998) 2664-2672.
- 566 [18] T. E. Lister, P. J. Pinhero, Scanning Electrochemical Microscopy Study of  
567 Corrosion Dynamics on Type 304 Stainless Steel, *Electrochem. Solid St.* 5  
568 (2002) B33-B36.
- 569 [19] T. E. Lister, P. J. Pinhero, The effect of localized electric fields on the detection  
570 of dissolved sulfur species from Type 304 stainless steel using scanning  
571 electrochemical microscopy, *Electrochim. Acta* 48 (2003) 2371-2378.

- 572 [20] Y. González-García, G. T. Burstein, S. González, R. M. Souto, Imaging  
573 metastable pits on austenitic stainless steel in situ at the open-circuit corrosion  
574 potential , *Electrochem. Commun.* 6 (2004) 637–642.
- 575 [21] R. M. Souto, Y. González-García, S. González, In situ monitoring of  
576 electroactive species by using the scanning electrochemical microscope.  
577 Application to the investigation of degradation processes at defective coated  
578 metals, *Corros. Sci.* 47 (2005) 3312-3323.
- 579 [22] E. Völker, C. González Inchauspe, E. J. Calvo, Scanning electrochemical  
580 microscopy measurement of ferrous ion fluxes during localized corrosion of  
581 steel, *Electrochem. Commun.* 8 (2006) 179–183.
- 582 [23] C. Gabrielli, S. Joiret, M. Keddad, H. Perrot, N. Portail, P. Rousseau, V.  
583 Vivier, A SECM assisted EQCM study of iron pitting, *Electrochim. Acta* 52  
584 (2007) 7706-7714.
- 585 [24] Y. Yin, L. Niu, M. Lu, W. Guo, S. Chen, In situ characterization of localized  
586 corrosion of stainless steel by scanning electrochemical microscope, *Appl.*  
587 *Surf. Sci.* 255 (2009) 9193-9199.
- 588 [25] J. J. Santana, J. González-Guzmán, L. Fernández-Mérida, S. González, R. M.  
589 Souto, Visualization of local degradation processes in coated metals by means  
590 of scanning electrochemical microscopy in the redox competition mode,  
591 *Electrochim. Acta* 55 (2010) 4488-4494.
- 592 [26] Y. González-García, J. J. Santana, J. González-Guzmán, J. Izquierdo, S.  
593 González, R. M. Souto, Scanning electrochemical microscopy for the

- 594 investigation of localized degradation processes in coated metals, Prog. Org.  
595 Coat. 69 (2010) 110-117.
- 596 [27] Y. Yuan, L. Li, C. Wang, Y. Zhu, Study of the effects of hydrogen on the  
597 pitting processes of X70 carbon steel with SECM, Electrochem. Commun. 12  
598 (2010) 1804-1807.
- 599 [28] N. Aouina, F. Balbaud-Célérier, F. Huet, S. Joiret, H. Perrot, F. Rouillard, V.  
600 Vivier, Single pit initiation on 316L austenitic stainless steel using scanning  
601 electrochemical microscopy, Electrochim. Acta 56 (2011) 8589-8596.
- 602 [29] A. J. Bard, M. V. Mirkin (Eds.), Scanning Electrochemical Microscopy, 1<sup>st</sup>.  
603 ed., Marcel Dekker, New York, NJ, 2001.
- 604 [30] M. Kaneko, H.S. Isaacs, Pitting of stainless steel in bromide, chloride and  
605 bromide/chloride solutions, Corros. Sci 42 (2000) 67-78.
- 606 [31] G. S. Frankel, Pitting Corrosion of Metals: A Review of the Critical Factors, J.  
607 Electrochem. Soc. 145 (1998) 2186-2198.
- 608 [32] M. Kaneko, H.S. Isaacs, Effects of molybdenum on the pitting of ferritic- and  
609 austenitic-stainless steels in bromide and chloride solutions, Corros. Sci. 44  
610 (2002) 1825-1834.
- 611 [33] E. A. Abd EI Meguid, N. A. Mahmoud, Inhibition of Bromide-Pitting  
612 Corrosion of Type 904L Stainless Steel, Corrosion 59 (2003) 104-111.
- 613 [34] A. Anderko and R. D. Young, Model for Corrosion of Carbon Steel in Lithium  
614 Bromide Absorption Refrigeration Systems, Corrosion 56 (2000) 543-555.

- 615 [35] D. S. Chau, B. D. Wood, N. S. Berman, K. J. Kim, Solubility of oxygen in  
616 aqueous lithium bromide using electrochemical technique, *Int. Comm. Heat*  
617 *Mass Transfer* 20 (1993) 643-652.
- 618 [36] D. D. Macdonald, The Point Defect Model for the Passive State, *J.*  
619 *Electrochem. Soc.* 139 (1992) 3434-3449.
- 620 [37] A. Di Paola, Semiconducting properties of passive films on stainless steels,  
621 *Electrochim. Acta* 34 (1989) 203-210.
- 622 [38] N.E. Hakiki, M.F. Montemor, M.G.S. Ferreira, M. da Cunha Belo,  
623 Semiconducting properties of thermally grown oxide films on AISI 304  
624 stainless steel, *Corros Sci* 42 (2000) 687-702.
- 625 [39] M.J. Carmezim, A.M. Simões, M.O. Figueiredo, M. Da Cunha Belo,  
626 Electrochemical behavior of thermally treated Cr-oxide films deposited on  
627 stainless steel, *Corros Sci* 44 (2002) 451-465.
- 628 [40] S. K. Sharma, *Green Corrosion Chemistry and Engineering: Opportunities and*  
629 *Challenges*, Wiley-VCH Verlag GmbH & Co., First Edition, Germany, 2012.
- 630 [41] M. S. Venkatraman, I. S. Cole, B. Emmanuel, Corrosion under a porous layer:  
631 A porous electrode model and its implications for self-repair, *Electrochim*  
632 *Acta* 56 (2011) 8192-8203.
- 633 [42] S. Thomas, I.S. Cole, M. Sridhar, N. Birbilis, Revisiting zinc passivation in  
634 alkaline solutions, *Electrochim Acta* 97 (2013) 192-201.

- 635 [43] S. Gao, C. Dong, H. Luo, K. Xiao, X. Pan, X. Li, Scanning electrochemical  
636 microscopy study on the electrochemical behavior of CrN film formed on 304  
637 stainless steel by magnetron sputtering, *Electrochim Acta* 114 (2013) 233-241.
- 638 [44] G. Lu, J. S. Cooper, P. J. McGinn, SECM imaging of electrocatalytic activity  
639 for oxygen reduction reaction on thin film materials, *Electrochimica Acta* 52  
640 (2007) 5172–5181.
- 641 [45] C. Song, J. Zhang, Electrocatalytic Oxygen Reduction Reaction, in: J. Zhang  
642 (Ed.), *PEM Fuel Cell Electrocatalysts and Catalyst Layers*, Ch. 2, Springer,  
643 London, 2008, p. 89.
- 644 [46] D. D. Macdonald, Passivity - the key to our metals-based civilization, *Pure*  
645 *Appl. Chem.* 71 (1999) 951-978.
- 646 [47] D. D. Macdonald, M. Al Rifaie, G. R. Engelhardt, New Rate Laws for the  
647 Growth and Reduction of Passive Films, *J. Electrochem. Soc.* 148 (2001)  
648 B343-B347.
- 649 [48] D. D. Macdonald, On the Existence of Our Metals-Based Civilization: I.  
650 Phase-Space Analysis, *J. Electrochem. Soc.* 153 (2006) B213-B224.
- 651 [49] C. Marconnet, Y. Wouters, F. Miserque, C. Dagbert, J. P. Petit, A. Galerie,  
652 Chemical composition and electronic structure of the passive layer formed on  
653 stainless steels in a glucose-oxidase solution D. Féron, *Electrochim. Acta* 54  
654 (2008) 123-132.

- 655 [50] S. Rhode, V. Kain, V.S. Raja, G.J. Abraham, Factors affecting corrosion  
656 behavior of inclusion containing stainless steels: A scanning electrochemical  
657 microscopic study, *Materials Characterization* 77 (2013) 109-115
- 658 [51] R.C. Newman, E.M. Franz, Growth and repassivation of single corrosion pits  
659 in stainless steel, *Corrosion* 40 (1984) 325-330.
- 660 [52] A.M. Simões, A.C. Bastos, M.G. Ferreira, Y. González-García, S. González,  
661 R.M. Souto, Use of SVET and SECM to study the galvanic corrosion of an  
662 iron–zinc cell, *Corros. Sci.* 49 (2007) 726-739.
- 663 [53] T. R. Beck, R. C. Alkire, Occurrence of Salt Films during Initiation and  
664 Growth of Corrosion Pits, *J. Electrochem. Soc.* 126 (1979) 1662-1666.
- 665 [54] Richard C. Alkire, Kai P. Wong, The corrosion of single pits on stainless steel  
666 in acidic chloride solution, *Corros. Sci.* 28 (1988) 411-421.
- 667 [55] A.C. Bastos, A.M. Simões, S. González, Y. González-García, R.M. Souto,  
668 Imaging concentration profiles of redox-active species in open-circuit  
669 corrosion processes with the scanning electrochemical microscope,  
670 *Electrochem. Commun.* 6 (2004) 1212-1215.
- 671 [56] H. Böhni, Localized Corrosion of Passive Metals, in: R. Winston Revie (Ed.),  
672 Uhlig's Corrosion Handbook, 2nd ed., Ch. 10, Wiley Interscience, New York,  
673 2000.
- 674 [57] R. Leiva-García, J. García-Antón, M.J. Muñoz-Portero Contribution to the  
675 elucidation of corrosion initiation through confocal laser scanning microscopy  
676 (CLSM), *Corros. Sci.* 52 (2010) 2133-2142.

- 677 [58] N.J. Laycock, R.C. Newman, Localized dissolution kinetics, salt films and  
678 pitting potentials, *Corros. Sci.* 39 (1997) 1771-1790.
- 679 [59] M. H. Moayed, R. C. Newman, The Relationship Between Pit Chemistry and  
680 Pit Geometry Near the Critical Pitting Temperature, *J. Electrochem. Soc.* 153  
681 (2006) B330-B335.
- 682 [60] P. Ernst, R.C. Newman, Pit growth studies in stainless steel foils. I.  
683 Introduction and pit growth kinetics, *Corros. Sci.* 44 (2002) 927-941.
- 684 [61] P. Ernst, N.J. Laycock, M.H. Moayed, R.C. Newman, The mechanism of lacy  
685 cover formation in pitting, *Corros. Sci.* 39 (1997) 1133-1136.
- 686 [62] D. Sun, Y. Jiang, Y. Tang, Q. Xiang, C. Zhong, J. Liao, J. Li, Pitting corrosion  
687 behavior of stainless steel in ultrasonic cell, *Electrochim. Acta* 54 (2009)  
688 1558-1563.
- 689 [63] J. Ren, Y. Zuo, The growth mechanism of pits in NaCl solution under anodic  
690 films on aluminum, *Surf. Coat. Tech.* 191 (2005) 311-316.

691

692

693 Table captions

694 **Table 1.** Electrochemical parameters for AISI 304 SS in both 0.2 and 0.6 M LiBr  
695 solutions, obtained from cyclic polarization curves

696

697

698 Figures captions

699 **Figure 1.** Cyclic voltammogram measured at the SECM tip of the AISI 304 SS in the  
700 0.2 M LiBr solution at 25 °C.

701 **Figure 2.** Approach curve for the tip polarized at  $-0.7 V_{\text{Ag}/\text{AgCl}}$  with the AISI 304 SS  
702 potential set at 0 V in the 0.2 M LiBr solution.

703 **Figure 3.** Cyclic potentiodynamic polarization curves for AISI 304 in both 0.2 and 0.6  
704 M LiBr solutions at 25° C.

705 **Figure 4.** SECM-3D maps of the AISI 304 SS surface biased at 0, 0.1 and 0.2  $V_{\text{Ag}/\text{AgCl}}$   
706 in the 0.2M (a) and 0.6M (b) LiBr solutions.

707 **Figure 5.** Line scans on a pit formed on the AISI 304 biased at  $0.45 V_{\text{Ag}/\text{AgCl}}$  in a 0.2 M  
708 LiBr solution.

709 **Figure 6.** Cyclic voltammogram measured near an active corrosion pit and initially at  
710 the SECM tip of the AISI 304 SS in the 0.2 M LiBr solution.

711 **Figure 7.** Current values at the tip current measured on an active pit at different  
712 polarization times.

713 **Figure 8.** Line scans on the AISI 304 maintained at open circuit potential at different  
714 repassivation times in the 0.2 M LiBr solution.

715 **Figure 9.** SECM-3D maps of the AISI 304 SS surface at the end of the pit activation  
716 process at  $0.45 V_{\text{Ag}/\text{AgCl}}$  (a) and at the end of the pit repassivation process at open circuit  
717 potential (b).



718 **Figure 10.** CLSM-2D image of a pit formed on the AISI 304 SS surface in the 0.2 M  
719 LiBr solution at 0.45 V<sub>Ag/AgCl</sub> (a). X and Y depth profiles are shown in (b) and (c),  
720 respectively.

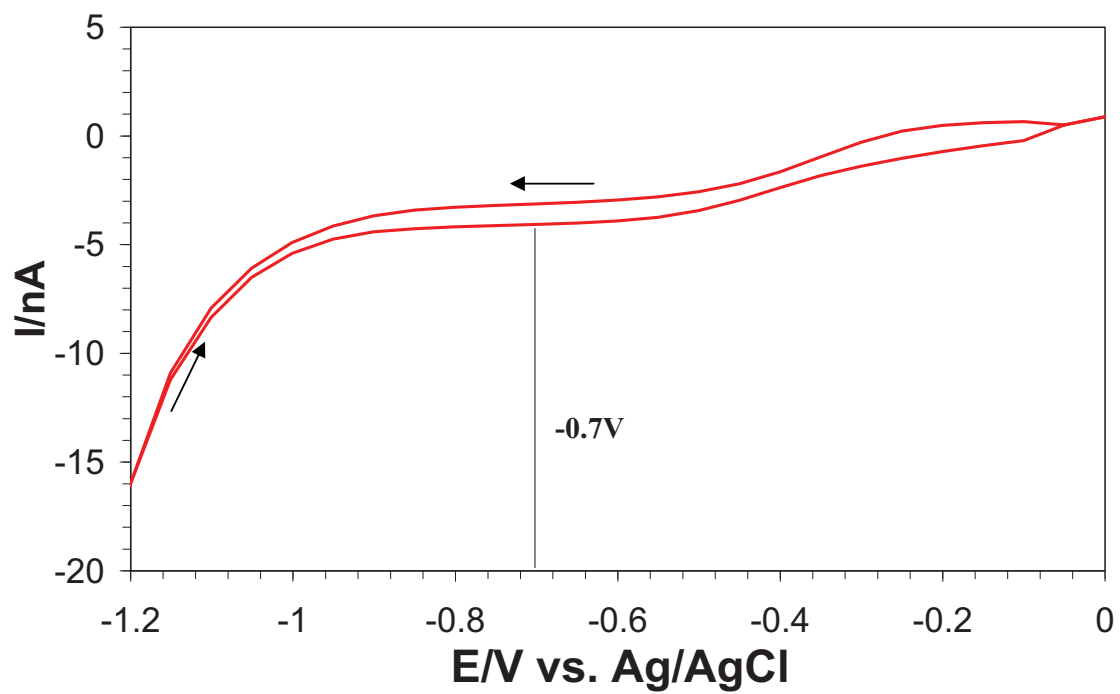
721

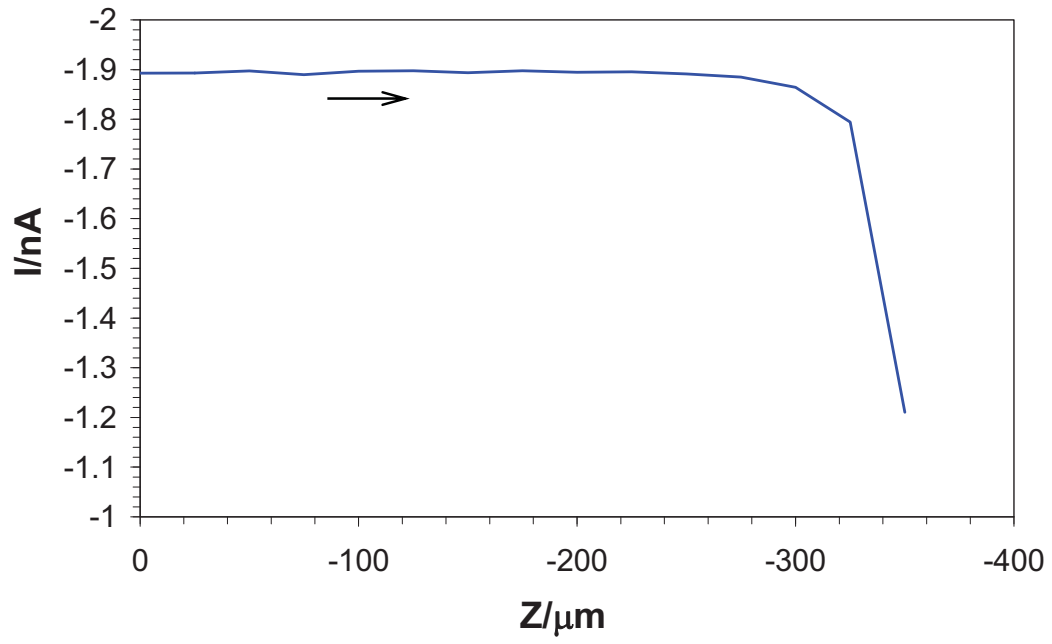
722

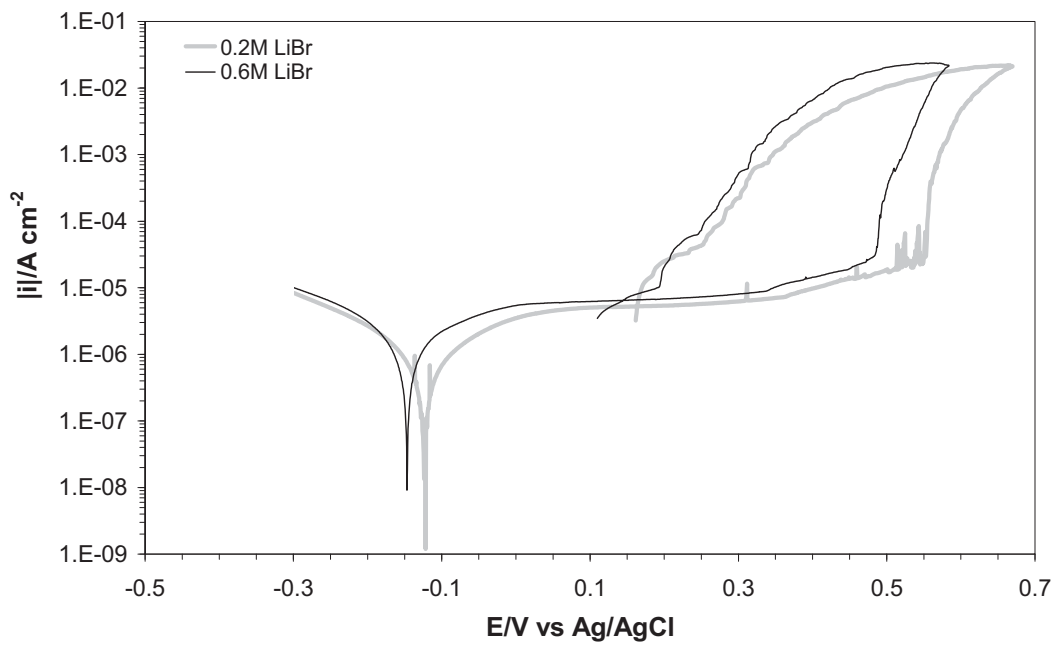
723

724

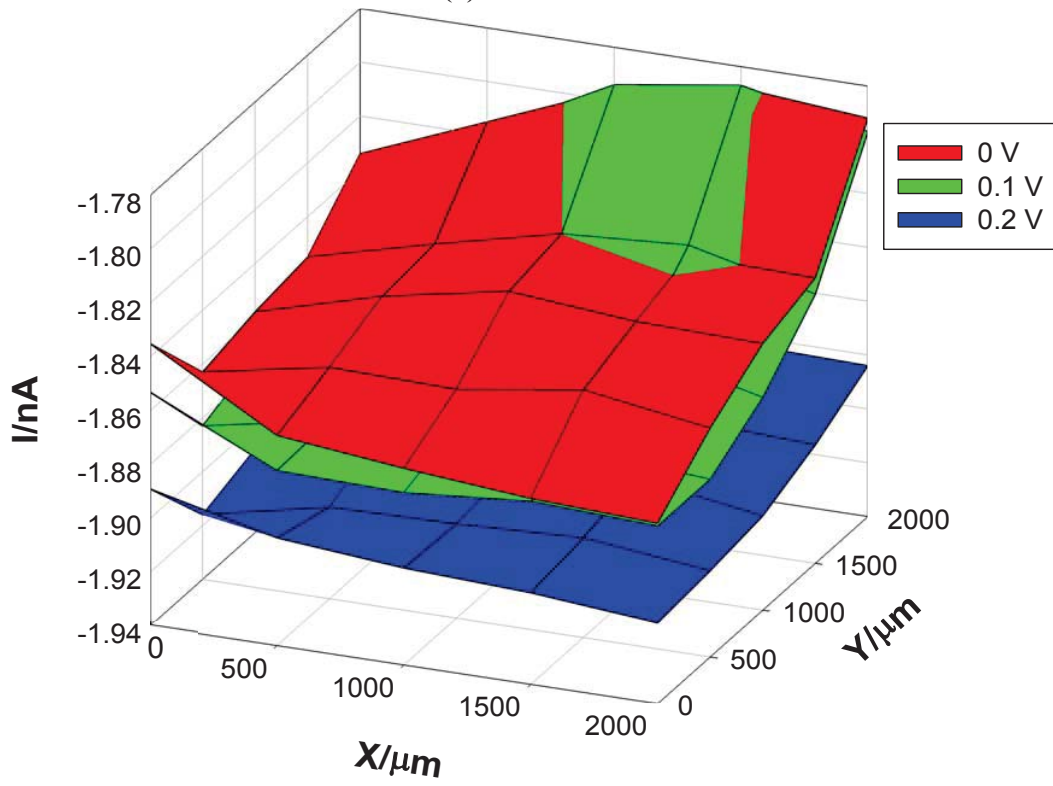
<b>LiBr Solution</b>	<b><math>E_{\text{corr}}/\text{mV vs (Ag/AgCl)}</math></b>	<b><math>i_{\text{corr}}/\mu\text{A cm}^{-2}</math></b>	<b><math>i_{\text{p}}/\mu\text{A cm}^{-2}</math></b>	<b><math>E_{\text{p}}/\text{mV vs (Ag/AgCl)}</math></b>	<b><math>E_{\text{rp}}/\text{mV vs (Ag/AgCl)}</math></b>	<b><math>i_{\text{rp}}/\mu\text{A cm}^{-2}</math></b>
<b>0.2 M</b>	$-124 \pm 7$	$0.3 \pm 0.1$	$2.3 \pm 0.2$	$557 \pm 10$	$164 \pm 10$	$5.3 \pm 0.1$
<b>0.6 M</b>	$-147 \pm 10$	$0.6 \pm 0.1$	$3.1 \pm 0.2$	$496 \pm 8$	$145 \pm 12$	$6.3 \pm 0.2$







(a) 0.2M LiBr



(b) 0.6M LiBr

